

The Cesium Physics Package Design for the PARCS Experiment

Eric A. Burt, William M. Klipstein
Jet Propulsion Laboratory
California Institute of Technology
Pasadena, California 91109

S.R. Jefferts
NIST – Time and Frequency Division
325 Broadway
Boulder, Colorado 80303

Abstract - The Primary Atomic Reference Clock in Space (PARCS) is a collaboration between the National Institute of Standards and Technology (NIST), the Jet Propulsion Laboratory (JPL) and the University of Colorado to build a laser-cooled cesium-beam atomic clock as a science payload for the International Space Station (ISS). The three primary goals of the PARCS experiment are (1) to demonstrate laser cooling of atoms in space, (2) to use laser cooling to build the most accurate space clock, and (3) to use the clock to test fundamental assumptions and predictions of relativity theory. In this paper we will discuss aspects of the PARCS cesium physics package subsystem design addressing magnetic, microwave and vacuum requirements as well as operational scenarios.

INTRODUCTION¹

The Primary Atomic Reference Clock in Space (PARCS) consists of a laser-cooled cesium atomic frequency standard designed to operate in the microgravity environment of the International Space Station (ISS) together with a GPS receiver used to facilitate frequency and time transfer. The frequency standard itself consists of several subsystems including, the Cesium Physics Package (CPP) where atoms are collected, cooled, launched, interrogated and detected; a Microwave Subsystem, which serves as a source of interrogation microwave signals, and the Laser and Optical Subsystem (LOS), which generates the optical beams used to collect, cool and launch atoms as well as state select them and detect them after microwave interrogation. Electronics, Avionics and Mechanical subsystems are integrated throughout the other subsystems. The CPP of the PARCS project consists of the vacuum chamber, including vacuum pumps, the microwave interrogation components attached to the vacuum chamber, and the magnetic shields and coils used

to control the magnetic environment. In this paper we will describe system engineering and design work performed for the CPP subsystem.

CPP CONFIGURATION

The conceptual design for the PARCS CPP has been described elsewhere [17, 18]. Fig. 1 shows a cross section of the CPP. Atoms are collected, cooled and launched from left to right. After passing a state selection region and then through two TE_{011} microwave cavities they are state detected in the region located in the far right of the figure.

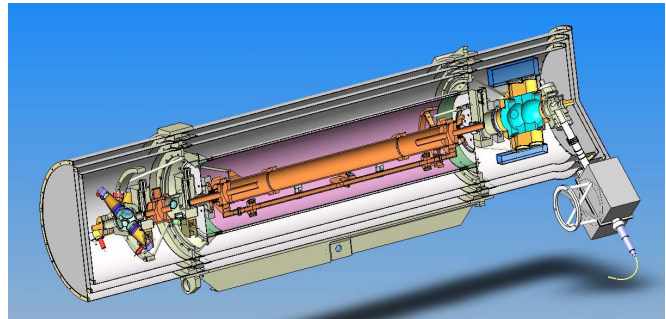


Figure 1. A cross section of the PARCS CPP. Four concentric cylindrical magnetic shields surround a vacuum chamber that includes the atom collection and state selection chambers on the left, the microwave interrogation chamber in the center and the detection chamber on the right.

Three atom shutters exist along the instrument bore to prevent light leakage into the microwave interrogation region while allowing multiple balls to be launched through the system concurrently. The vacuum chamber has a minimum diameter of 1.5 cm along its entire length. The design must operate over a range of launch velocities between 30 cm/s (multiple balls launched at 1.2/s) and 15 m/s (single balls, atom shutters remain open). Normal operation occurs at the lower velocity, while the faster launch velocities are used during diagnostic tests such as determination of the end-to-end phase shift and measurements of the magnetic field.

¹ Part of the research described in this paper was carried out at the Jet Propulsion Laboratory, California Institute of Technology, under a contract with the National Aeronautics and Space Administration. Part of the research described in this paper is work of the United States government, not subject to US copyright.

Atoms are launched from the titanium collection chamber using 6 optical beams in a 1,1,1 geometry. Each beam has a 1 cm $1/e^2$ Gaussian radius determined by a bolt-on fiber collimator and delivers 5 mW. Repump light is delivered by a separate collimator. The optical windows provide a 3 cm clear aperture. See Ref. [22] for a description of both the optical windows and the spill-proof cesium source. A polycrystalline graphite tube is placed at the exit of the collection chamber and two annular polycrystalline graphite disks are placed in the state selection region to limit migration of background cesium outside of the collection region. After being launched, atoms pass through an atom shutter into the state selection region, which consists of a low-Q titanium microwave cavity followed by a “push” beam used to remove non-state-selected atoms. After passing through a second atom shutter, atoms enter the microwave interrogation region, which consists of a coupling structure and two Ramsey cavities separated by 75 cm. This distance results in a Ramsey time of 2.5 s at the nominal 30 cm/s launch velocity. After the interrogation region is a third atom shutter followed by the detection region. This consists of two beams for detection (one primary and the other for normalization) along with a push and a repump beam. The detection beams are σ^+ standing wave sheets 1.7 cm wide (transverse direction) by 4 mm thick (axial direction) while the push beam has the same dimensions but is traveling wave and the repump beam is 1.7 cm wide by 1 mm thick.

Light Control: Atom Shutters

The PARCS prototype atom shutters, shown in Fig. 2 are built out of titanium, are UHV-compatible, non-magnetic and piezo-electric transducer (PZT)-actuated. The PZTs are located outside of the vacuum and the long lever arms connecting them through a titanium membrane vacuum wall translate their micron-scale motion into the required 1.5 cm open aperture of the shutter blades.

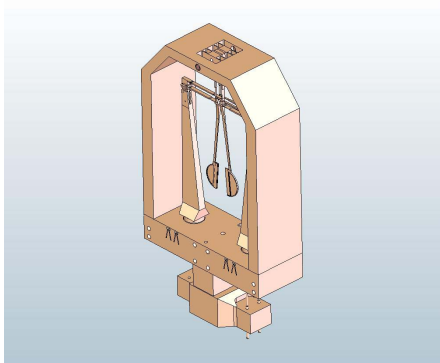


Figure 2. A perspective view of the prototype PARCS atom shutter.

One shutter blade is a knife-edge that fits into, but does not touch, a pocket formed by two knife edges on the second blade. When the first blade is inserted into the pocket of the second with an overlap of 0.75 mm, the prototype attenuates light leakage to 2×10^{-9} of the light impinging on the shutter (Fig. 3).

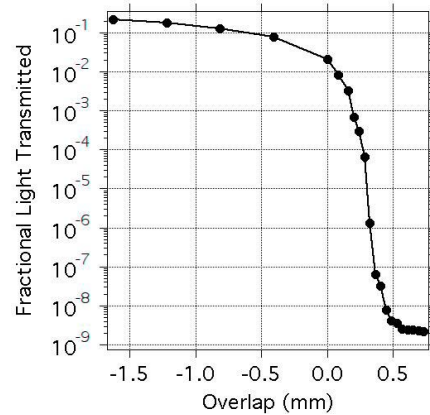


Figure 3. Atom shutter light attenuation.

A further factor of 20, bringing this attenuation factor to the required 10^{-10} , is anticipated by adding light baffles around the shutter mechanism, increasing the blade overlap by 0.5 mm and coating surfaces with a non-reflective material such as graphite (eg., aerodag). Analysis and tests show that stray light from the various CPP light sources can be attenuated to 10^{-6} before reaching the atom shutters. This together with the attenuation provided by the atom shutters will reduce light leakage into the interrogation region to less than the 10^{-14} mW/cm² requirement.

The shutter actuation time is 15 ms. A shutter life (determined by expected operation during mission life and ground testing) is defined to be approximately 2.1×10^7 cycles. The prototype shutter has passed 3 lives (6.3×10^7 cycles) of continuous operation.

MAGNETIC FIELD CONTROL

Magnetic Shielding Requirements

Strict control of the magnetic field in the CPP is required for normal operation. The PARCS accuracy goals allow for a budget on the fractional frequency shift due to the second order Zeeman shift of 2×10^{-17} . The magnetic field in the interrogation region will be periodically measured, but between measurements, the field must not vary in such a way as to cause a fractional frequency shift larger than this value. The variation in the second order Zeeman shift with magnetic field variations for the $F=3, m_f=0$ to $F=4, m_f=0$ transition in cesium is, $(\Delta f/f)_Z = 9.299 \times 10^{-8} B_0 \Delta B$, where B_0 is the C-field in Gauss and ΔB is the fluctuations in that field in Gauss. For a C-field of 300 μ G, we see that ΔB must be held less than 0.7 μ G. Simulations (source: IGRF2005) show that for site 11 on the ISS JEM-EF (the anticipated location for the PARCS instrument), the ambient fields can vary by as much as ± 0.5 Gauss across an orbit, thereby requiring a shielding of about 10^6 . Given spatial and mass constraints, passive shielding alone will not be able to reach this level. Therefore PARCS will have a combination of active and passive shielding. The active shielding will be implemented as a feed-forward lookup table as described below.

In addition to shielding out fluctuations in the magnetic field, the CPP magnetic control must provide specific field values in various locations. The atom collection region, which is inside of magnetic shield 2 (MS2 – shields are numbered inside to out) and outside of MS1 must have a field magnitude less than 1 mG and a gradient of less than 0.1 mG/cm. These values facilitate laser cooling of the collected atoms. The state selection region, also inside MS2 and outside MS1 will require a field settable from 1-100 mG. The microwave interrogation region will have a field settable between 30 μ G to 3 mG and a time rate of change less than 1 nG/s. From the state selection region to the exit of the microwave interrogation region, all field gradients must be consistent with adiabaticity requirements. The question of magnetic adiabaticity will be taken up in its own section below.

Passive Magnetic Shielding

The CPP design for passive shielding employs a set of 4 concentric cylindrical shields with the geometry shown in Fig 1. MS1 contains the microwave interrogation region with its endcaps closing approximately 5 cm before the entrance to Ramsey cavity 1 and 5 cm after the exit from Ramsey cavity 2. MS2 contains all other parts of the CPP except the ion pump, which is positioned outside of MS4.

The space available for the CPP constrains the spacing between shield layers to be small compared to their radii. Thus the results of Gubser [1] apply and we have a functional form to estimate shielding effectiveness. Using Gubser's results and checking with a finite element model, we find that shield mass and shielding effectiveness are optimized as mass is moved inward to MS1. The results of this optimization are shown in Table 1. With a realistically achievable mu-metal permeability, the model predicts a shielding effectiveness for this configuration of 2×10^5 . A prototype shield set with similar geometry designed for the PARCS testbed fountain [22] achieved a measured shielding factor of 1.4×10^5 .

Table 1
Optimized magnetic shield dimensions

Shield	Radius (cm)	Length (cm)	Thickness (cm)
MS1	11.2	89.7	0.32
MS2	13.4	155	0.1
MS3	16.2	164	0.1
MS4	20.3	168	0.08

Environmental Tests of Mu-Metal Magnetic Shields

In space, the PARCS magnetic shield set will be subjected to a harsher environment than would a typical laboratory shield set. Several tests were carried out to determine the mu-metal response to this environment.

A prototype shield set exhibited no "gaussing" near its walls at the 1 μ G level when subjected to $\sim 7,000$ cycles of a sinusoidally varying external field with amplitude 0.3 G (simulating 6 experiment lifetimes of ISS orbits). No impact on shielding was observed during this test either. The same shield set exhibited a temperature coefficient of $-0.6 \mu\text{G}/\text{C}$ measured on axis when subjected to an external temperature varying slowly from 15 to 35 C. An anticipated temperature

stability of $< 0.1 \text{ C}$ will result in fluctuation well below the required limit of $0.7 \mu\text{G}$.

To test the effect on mu-metal of mechanical vibrations similar to those expected in a shuttle launch, a two-layer cylindrical shield set was subjected to a series of vibration levels, while the local fields next to the shield walls and the axial shielding effectiveness were monitored. The DC field at the location of the shields on the vibration table with the solenoids energized, but with the table stationary was less than 1 G. The AC fields with the table vibrating at 40 grms from 20 to 2000 Hz were less than 2.6 Grms. The table was vibrated at 3.75, 7.25, 11 and 19 grms with a flat spectrum from 20 to 2000 Hz. Some of the results of the vibration testing are shown in Fig. 4. 11 grms is the vibration level that the CPP shield set will experience during a shuttle launch.

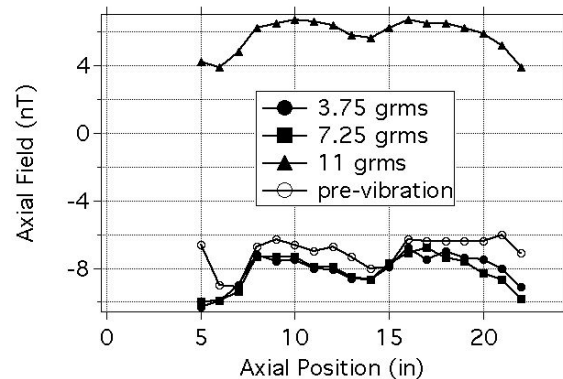


Figure 4. The magnetic field measured along the axis of a two-layer cylindrical magnetic shield set before and after various vibration levels.

A change clearly occurred at the 11 grms vibration level corresponding to a peak stress of 1500 psi. This value is an order of magnitude less than the proportional limit for mu-metal (about 18,000 psi), and demonstrates that the magnetic properties of mu-metal can change well below this limit. Degaussing the shields failed to restore the field to its pre-vibration values. The change appears to have occurred uniformly throughout the shield and if typical, could be taken out by applying a bias to the C-field. While there was a small shift in the field values, axial shielding effectiveness was completely unchanged by all vibration levels.

Active Magnetic Shielding

Some form of active shielding is required to reach the overall required shielding factor of 10^6 . Feedback control was considered, but typically resulted in good shielding only at a point, while often leading to degradation elsewhere. A feed-forward method that uses an external axial probe located at the center of one of the MS4 endcaps and an axial compensation coil wrapped on the outside of MS3 was found to work best. The feed-forward lookup table for the shield set is determined empirically in the following way. The shield set is placed within a large ($\sim 2 \text{ m}$ diameter) 3-D Helmholtz coil set that can be used to simulate the varying (rotating) field on the ISS. For each change in the external field orientation, the *external* axial field at the sensor and the current applied to the compensation coil that results in the minimum change in the *internal* axial

field inside MS1 (measured with a temporarily located internal probe) as compared to the previous external field setting are recorded. The results of compensation current vs. external axial field are fit to a second order polynomial to obtain an approximate functional form. The functional form is then used to determine the compensation current for an arbitrary axial external field component and the internal probe can be removed. Essentially, this method is nulling the effect of axial fluctuations in the external field, while taking advantage of the asymmetrically large transverse shielding already available in long mu-metal cylinders.

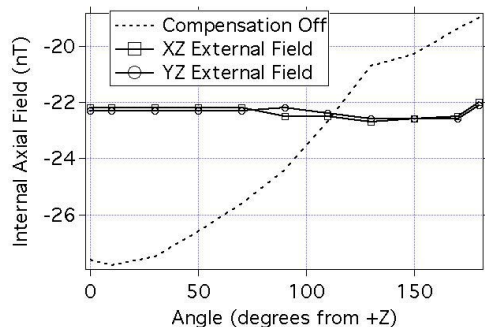


Figure 5. The axial field inside of the shield set as a function of external field orientation. The graph shows how the internal field varies with and without compensation. With compensation on, the orientation is rotated through 180 degrees in two orthogonal planes, XZ and YZ with almost identical results.

Fig. 5 compares the variations in the internal field with and without this type of compensation. The results are similar over 80% of the length of the internal shield and the lookup table, along with its fit, is robust against degaussing and re-orientation of the shields. The reduction in internal field variations is almost an order of magnitude. The combination of this together with passive shielding on the order of $1-2 \times 10^5$ will achieve the 10^6 overall shielding requirement.

End-to-end Field Model

Fig. 6 shows the field magnitude along the axis of the CPP determined from a finite element model for both orbital extremes of the external magnetic field. The model suggests that the requirements on field magnitude will be met in the various CPP locations. However, the gradient just after the state selection region, which impacts adiabaticity, requires further work. In addition, while field uniformity requirements are met for a single external field value, the extreme variations in the external field during ISS orbits destroy that uniformity as shown in Fig. 7 for the microwave interrogation region. The model included passive shielding and coils in the state selection and interrogation regions turned on to nominal values, but no active shielding and no adiabaticity compensation (see below).

The state selection coil is a solenoid with radius 10.5 cm and length 4.4 cm centered axially on the state selection microwave cavity. It consists of 2 windings of 10 turns each such that 0.5 mA of current results in a field of about 1.3 mG at its center. The C-coil has a 10.5 cm radius, 88.1 cm length and has 70 turns total in two layers. It is centered axially on

the microwave interrogation region, extending approximately 5 cm beyond the end of each cavity. A current of 0.58 mA results in a C-field of about 300 μ G.

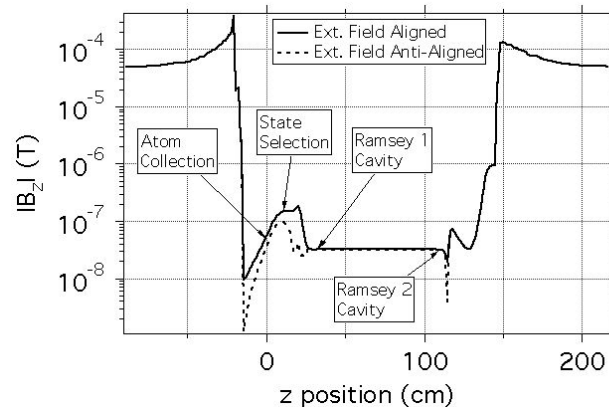


Figure 6. The graph shows the magnitude of the axial magnetic field inside the CPP as a function of axial position. The internal field is shown for both extremes of the external field due to ISS orbit. Identified in the graph are the atom collection region centered at 0 cm, the state selection region centered at 10.7 cm, the entrance to the first Ramsey cavity at 31.5 cm and the exit from the second Ramsey cavity at 108.7 cm. For reference, the entrance to MS1 is at 25.5 cm and the exit from MS1 is at 115 cm.

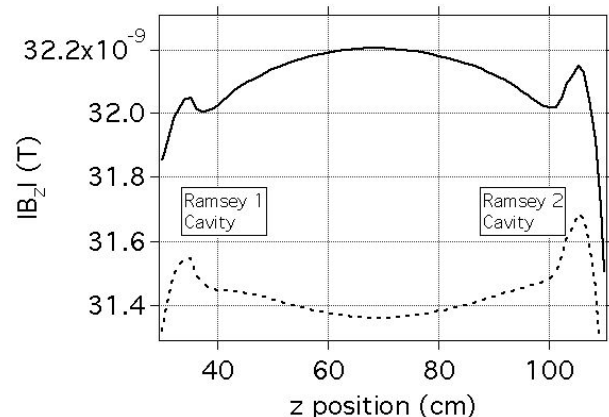


Figure 7. A detail of the field in the microwave interrogation region showing the variation in the field across an orbit. The solid line corresponds to the external field oriented in one direction, while the dashed line corresponds to the opposite orientation.

Two shim coils with approximately Helmholtz geometry are wrapped on the outside of each Ramsey cavity to fine tune the fields there and ameliorate edge effects in the field of the C-coil. The Ramsey shims have radii 3.6 cm, separation 3.5 cm, and consist of 1 turn each. Modeling suggests that between 10-20 μ A of current is required for each coil pair to minimize fringing in the fields near the cavities. In addition there is a “follow” coil located at the entrance to MS1, which will be described in the “Magnetic Field Adiabaticity” section and a “Zeeman” coil described in the “In-Flight Magnetic Field Measurement” section.

Magnetic Field Adiabaticity

After atoms leave the state selection region they are in the $F=3, m_F=0$ state and any change in that state not due to

microwave interrogation will cause errors in clock performance. Adiabaticity refers to the ability of the atomic magnetic moment to follow a changing magnetic field without changing state. The adiabatic ratio is defined as $R = \omega_L B / (v |dB/dz|)$, where $\omega_L = \Delta m_F g_F \mu_B B / \hbar$ is the Larmor frequency of the atomic magnetic moment ($g_F = -0.25$ for cesium $F=3$, μ_B is the Bohr magneton, B is the magnitude of the external field and \hbar is Planck's constant), dB/dz is the field gradient and v is the atom velocity, which converts the gradient into a time dependence. The field is adiabatic if $R \gg 1$. Adiabaticity is easily achieved for the normal launch speed of 30 cm/s. However, to resolve the individual m states in the state selection cavity at the highest atom launch speed of 1500 cm/s and thereby perform efficient state selection without degradation due to transit-time broadening, we must have $B \geq 4\hbar v / (\mu_B l)$ in the state selection region. For the fast launch speed this corresponds to several mG. In contrast, due to its quadratic dependence on the field, the second order Zeeman shift drives the C-field to low values (0.3 mG or less to remain within the PARCS accuracy budget with expected fluctuations). Consequently there is necessarily a field gradient between the two regions.

It can be shown that optimal adiabaticity is achieved by a field that has a $1/z$ dependence (the z direction is along the axis of the CPP) [2]. Fig. 8 shows the modeled correction to the field going across the endcap of MS1 where adiabaticity is most difficult to achieve.

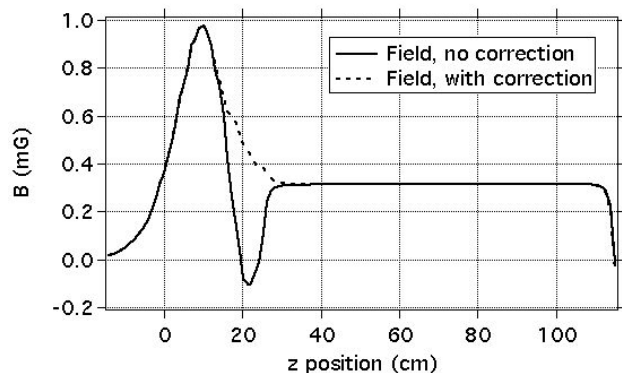


Figure 8. The magnetic field magnitude as it crosses the entrance to MS1 at about 20 cm.

The solid line shows the field with no adiabaticity compensation, while the dashed line shows an approximately $1/z$ dependence near the endcap. This compensation is achieved by placing a solenoid of length 9.1 cm, radius 1.25 cm and centered at 21.1 cm. A second coil is wrapped on the outside of this solenoid at its center. Windings and current on the solenoid are such as to provide 0.38 mA/cm. The second coil has a total of 0.32 mA. The solenoid located with one end penetrating the MS1 endcap by about 1 cm. Fig. 9 shows the resultant adiabatic ratio. The minimum value of 10 achieved in this way is only marginally “much greater than 1”. While acceptable at this stage of the design process, given the boundary conditions, it is a theoretical best and further

improvements can only be obtained by changing those boundary conditions.

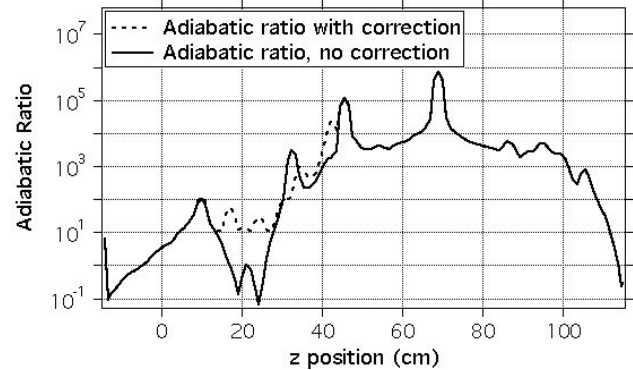


Figure 9. The adiabatic ratio with and without the $1/z$ correction for the 1500 cm/s atom launch speed.

In-Flight Magnetic Field Measurement

Typically a field-dependent hyperfine transition is used to measure the C-field. However, in the PARCS CPP the long interrogation time leads to a very narrow Rabi pedestal. Even a relatively small field inhomogeneity in the interrogation region could wash out the Ramsey fringes or move them off the Rabi pedestal. To measure the magnetic field in PARCS we will use a transverse coil in the free-precession region (referred to as the “Zeeman coil”) to drive low frequency Majorana transitions instead [3]. The Zeeman coil will be wrapped on the outside of the C-field coil.

Ion Pump Magnetic Field Measurement and Modeling

A contour map of the ion pump magnetic field was constructed to determine whether this field could cause magnetic shield saturation. Values as high as 6.5 Gauss at the MS4 surface, 3.8 cm from the pump flux return, were measured. Such fields are an order of magnitude larger than ambient fields and are of the approximate magnitude to cause local saturation in the shield material. The impact of this field was determined by measuring the shielding effectiveness of a shield set as an ion pump magnet was brought in from a large distance. As the magnet approached the design distance, the shielding effectiveness changed slightly indicating the onset of saturation. There is no room to move the pump further away so the CPP will employ a second 1.6 mm thick mu-metal flux return located 0.5 cm outside the first. Modeling shows that the resultant flux leakage is reduced by a factor of 8x bringing it almost to ambient levels at MS4.

VACUUM CHAMBER

Vacuum Requirements

The requirements on vacuum pressure in the CPP are listed by region in Table 2 along with modeled values for the CPP design. The model treats the vacuum enclosure as a network of chambers connected by conductance tubes. Each chamber has an outgassing rate for each gas, a pumping speed out due to various pumps and a gas flow in from all adjacent

chambers. Some care was taken to compile reasonably accurate data on these parameters as described below.

Table 2
CPP vacuum pressure requirements and modeled values.

Item	Requirement	Modeled Value
Cs partial press. in collection chamber	$10^{-8} - 10^{-10}$ Torr	$10^{-8} - 10^{-10}$ Torr
Other pressure in collection chamber	$< 10^{-10}$ Torr	5.7×10^{-11} Torr
State selection background pressure	$< 5 \times 10^{-11}$ Torr	1.6×10^{-11} Torr
Microwave interrogation region pressure of CH ₄ and C _n H _{2n+2}	$< 1 \times 10^{-11}$ Torr*	3.7×10^{-12} Torr
Microwave interrogation region background pressure of other gasses	$< 5 \times 10^{-11}$ Torr	3.9×10^{-11} Torr
Cs partial press. in detection region	$< 1 \times 10^{-12}$ Torr	$\ll 1 \times 10^{-12}$ Torr
Other press. in detection region	$< 5 \times 10^{-11}$ Torr	8.1×10^{-12} Torr
Number of cesium atoms in detection region contributing to signal	$< 10^3$	~ 100
Number of cesium atoms in detection region contributing to background	< 600	~ 100

*The pressure shift in cesium due to CH₄ is $-1.040(5) \times 10^{-7}$ /Torr [4].

Vacuum Chamber Materials and Outgassing

The bulk of the CPP vacuum chamber is constructed out of titanium and copper with quartz used for optical windows. In the model, outgassing rates for the most common UHV gasses, CO, CO₂, H₂, O₂, He, N₂ and CH₄ [8, 14-16] are incorporated. All of these are dominated by H₂ by one to two orders of magnitude. The outgassing rate for H₂ from titanium is taken to be 7×10^{-14} torr-l/s-cm² and for copper, 2×10^{-14} torr-l/s-cm² [14]. The diffusion rate for He through quartz is taken to be 2×10^{-14} torr-l/s-cm². An upper bound on the outgassing rate from a typical weld for an object the size of a 7 cm (2.75") CF component is estimated to be 2×10^{-12} torr-l/s based on known vacuum systems and associated pressures. Similarly an upper bound on the leak rate of a typical 7 cm (2.75") CF flange is taken to be 1×10^{-13} torr-l/s, again derived from known vacuum systems with known pressures. Virtual leaks are not accounted for in the model as they can take on any value. Best practice for avoiding them will be employed in the design and assembly of the CPP.

Pumps, Pumping Speeds and Conductance

Pumps considered in the model include ion pumps, non-evaporable getters (NEGs), polycrystalline graphite getters (PGGs) and TiVZr getter films (GFs) with pumping speeds listed in [10] and [11]. In addition, PGGs (eg., Poco sintered graphite CZR-2) are able to absorb 200 mg of cesium per 1 g of getter [5] and are used to contain cesium in the collection region. The sticking coefficient for cesium on this getter material varies with temperature and age. At room temperature it is initially as high as 0.9 but degrades with time. A conservative value of 0.5 is used here.

For conductance tubes with simple geometries, stock formulae for conductance are used [12]. For more complex geometries a Monte-Carlo simulation provides more accurate results [13]. The conductance through each of the 3 atom shutters is de-rated by their duty cycles.

End-to-end Vacuum Model

In the model the base pressure in the i^{th} chamber for a given gas is determined by the equation:

$$R_i + (P_{i1} - P_i)C_{i1} + (P_{i2} - P_i)C_{i2} + \dots = 0,$$

where R_i is the total outgassing rate in chamber i for the desired gas, P_{i1} is the pressure in the first chamber adjoining chamber i , P_{i2} is the pressure in the second chamber adjoining chamber i (and so on), P_i is the pressure in chamber i , C_{i1} is the conductance between chamber i and the first chamber adjoining chamber i (and so on). A steady state is assumed so that all rate equations are set equal to 0. Several pump configurations were modeled. The configuration that did the best job of balancing complexity against meeting requirements consisted of a 20 l/s ion pump located near the state detection region, a NEG tube located at the exit of the atom selection region, PGG annular disks located at the entrance and exit of the state selection region and a NEG located near the ion pump (largely as a backup for that pump). Fig. 10 shows the estimated base pressure for this configuration along with the requirement by region. For technical reasons, it is only practical to apply the GF in the interrogation region. There it dramatically improves the base pressure, but due to conductance limits, this pump combination fails to meet requirements in some other regions. Since GFs are difficult to apply and are not required to meet the vacuum requirements, they are not used in this design.

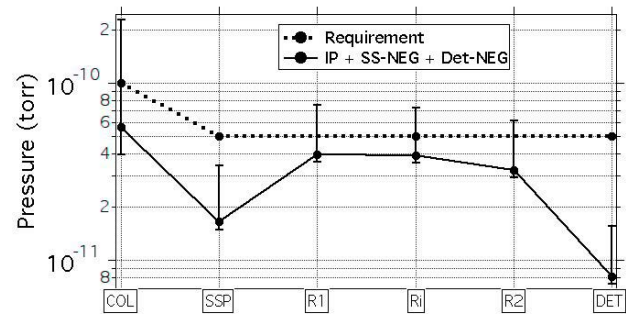


Figure 10. Vacuum chamber base pressure modeling results. The solid line corresponds to the modeled values and the dashed line is the requirement. The regions indicated are, COL = atom collection, SSP = state selection push, R1 = Ramsey cavity 1, Ri = free precession, R2 = Ramsey cavity 2 and DET = state detection region. Error bars are derived by varying the (already conservative) weld outgassing and flange He leak rates (the two values with the most uncertainty) by a factor of 10 in either direction.

Ion Pump Vibration Testing

Ion pumps are flown on the shuttle regularly, however to the best of our knowledge, a Varian star cell pump (or equivalent – preferred for its noble gas pumping characteristics) has never been flown or qualified for flight. Since the internal filament structure in a star cell pump is different than in other ion pumps, we performed a 3-axis random vibration test of a 20 l/s star cell pump as a first step towards flight-qualification. The vibration levels used in this test are appropriate for a shuttle launch and are listed in Table 3.

Table 3
Vibration levels used for ion pump vibration test. This vibration spectrum was repeated for each direction.

Frequency (Hz)	ASD
20	0.0125 g ² /Hz
20 – 80	+6 dB/Octave
80 – 600	0.20 g ² /Hz
600 – 2000	-4.5 dB/Octave
2000	0.033 g ² /Hz
Overall	14.8 g _{rms}

After each vibration level, pump functionality was determined by monitoring pump current. This value, with an equivalent resolution of 2×10^{-10} torr pressure, remained unchanged throughout the test. In addition, post-vibration x-rays revealed no signs of changes or damage in the internal structure of the pump.

MICROWAVE INTERROGATION

Microwave Requirements

PARCS operation calls for the two microwave cavities to be operated in phase and 10 half linewidths detuned from the atomic resonance coupled by a common resonant structure [18]. Since PARCS is intended to operate in a micro-gravity environment, the two microwave interrogations are separated in space to accommodate the drifting atoms. This separation re-introduces the end-to-end cavity phase shift absent in laser-cooled fountain clocks. The end-to-end cavity phase shift will be periodically measured, but in between measurements the change in the shift can be no more than 15 μ radians to support an overall accuracy goal of less than 10^{-16} . This requirement drives the microwave interrogation region in several ways.

The fractional frequency shift due to an end-to-end cavity phase difference is given by $(\Delta f/f)_{ETE} = -\Delta\phi\nu/(2\pi fL)$ where $\Delta\phi$ is the phase difference, ν is the atom velocity and L is the distance between cavities. To measure this effect we take advantage of its linear dependence on ν and periodically operate the clock at several different velocities [17]. Once this measurement is made a correction can be applied, but the phase difference must be no larger than 15 μ radians between measurements to avoid degradation in accuracy. If the cavity were operated on-frequency this would require μ K-scale temperature control. Instead the cavity is operated 5 linewidths (FWHM) off resonance where the phase temperature coefficient is much lower [18]. A stability of 2 mK in the difference between the temperatures of the two cavities is sufficient and requires no degradation in Q. Microwave interrogation will use phase modulation as described in [19] and [17].

The distributed cavity phase frequency bias is an effect due to spatial variations in the microwave phase within the cavity. It is largely due to resistive losses in the cavity walls, imperfections in cavity fabrication and imbalances in cavity feed power. It is well known that the distributed cavity phase due to wall and endcap resistivity varies quadratically in the axial direction [23, 24]. A numerical simulation of Bloch vector evolution using the PARCS microwave interrogation region parameters, a quadratically varying longitudinal

microwave phase and a half-sine varying microwave amplitude indicates that at normal power a phase difference of 70 μ radians at the endcaps relative to the cavity center will result in a 2×10^{-17} fraction frequency bias. Ref. [23], which numerically calculates the distributed cavity phase using a finite element approach, shows that this condition is approximately met. The PARCS cavity design also uses a 4-port feed system and interior dimensions are machined to ± 5 μ m tolerance. The distributed cavity phase frequency bias also depends on microwave power [21]. Since the cavity is operated 5 linewidths off resonance, 100x more microwave power is required. A distributed cavity phase shift due to geometric changes (for instance, wall irregularities due to machining imperfections) is not amplified by the 100x power increase because it is geometric in nature [18]. An analysis of the requirements on port balancing shows that even with the higher power, these should not be difficult to meet [18]. Other power-dependencies of the distributed cavity phase are under investigation [21]. Finally it is essential that all of the requirements on the microwave subsystem survive the 200 C vacuum bakeout required by the vacuum subsystem. This requirement will lead to a new microwave cavity fabrication method described below.

Microwave Interrogation Region Modeling and Design

Finite element modeling of the cavities and their coupling structures estimate that a reflection coefficient of 0.9 at the cavity coupling ports together with a coupling port size of 8 mm (well into weak-coupling) and a resonant coupling structure gives an optimal compromise between maximal Q and maximal power coupled into the cavity along with minimal sensitivity to changes in coupling waveguide length. This model predicts a phase temperature coefficient of 7 mrad/K for a temperature differential between cavities. A 2 mK relative temperature stability is required to maintain <15 μ rad phase difference between cavities.

The microwave interrogation signal is routed from the Microwave Subsystem to the CPP by coaxial cable. At the CPP, the signal is coupled into a resonant waveguide structure as described in [18]. With this structure, it was found that the end-to-end phase difference varies as 0.785 mrad/mm. From this we derive a dimensional tolerance of about 19 μ m and it can be seen that temperature stability on the coupling structure will not be a problem (a 0.2 K change in temperature leads to a 2 μ m length change). The “T” between the two arms of the coupling structure is tunable so as to provide a mechanism for taking out residual machining errors.

Each cavity has a radius of 3 cm and a length of about 2.2 cm. To achieve a standing wave pattern and to decrease phase variations inside the cavities, they each have 4 microwave feeds. It is essential that each feed supply the same signal (frequency, phase and power) to the cavity. Due to finite losses in the coupling structure, the path length to each coupling port must be identical. The PARCS CPP cavities will use a two-layer coupling structure attached to the coupling ports that provides a complete symmetry for all four paths. See Fig. 10. The main microwave coupling arms have UHV-compatible ceramic microwave windows and a non-

vacuum microwave-tight breakable seal for assembly. A window and breakable seal pair is symmetrically placed in each arm.

Cavity cross section as viewed along axis

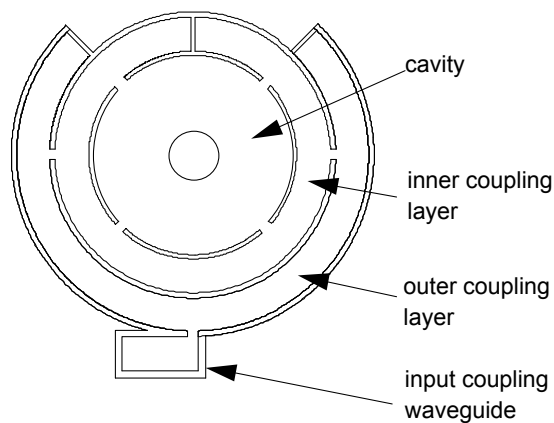


Figure 10. The microwave cavity cross section at the axial midpoint as viewed along its axis. Microwaves from the input coupling waveguide make a 90 degree turn by passing through an offset feed (“input coupling waveguide”) into the outer coupling layer. From there they propagate in opposite directions until they reach two symmetrically placed ports connecting the outer coupling layer to the inner coupling layer (each coupling layer is similar to WR90 waveguide). Microwaves are again split in two directions at each port and reach two more symmetrically placed ports connecting the inner coupling layer into the cavity itself. In this way, the coupling structure provides identical path lengths for each of the four microwave feeds into the cavity.

Prototype Microwave Cavities

Two prototype microwave cavities were built to test the fabrication procedure (see below) and to test the predictive power of the models used to analyze cavity characteristics. Predicted and measured cavity mode frequencies were in good agreement for both cavities. In addition to the clock TE_{011} mode, the TM_{111} mode is particularly interesting because in a simple cylindrical cavity the two modes are degenerate and the TM_{111} mode will drive the wrong transitions. The degeneracy is usually broken by attaching two ring-shaped quarter-wave gaps to the outside radial edge of each endcap of the cavity. There is significant H field in the TM_{111} mode at this location so this mode couples with the gaps and is shifted by them. The H field of the TE_{011} mode is very small there and it remains unaffected. The addition of the gaps (“mode filters”) splits the TM mode into two parts – one shifted up and the other shifted down in frequency. The amount of shift is a function of the mode filter depth so in the model the depth was varied to look for the expected dependence and remove uncertainty in mode identification. However, in addition, this analysis revealed that the relative large input and output chokes themselves shift the TM mode while having little effect on the TE mode. The model predicts that the chokes alone will shift the TM mode by 370 MHz (Fig. 11). Since this sufficiently breaks the degeneracy, future cavities may eliminate the mode filters altogether, thereby simplifying

fabrication. With the quarter wave filters in place, the upper TM mode is at 9.6 GHz, while the lower TM mode is at 7.5 GHz.

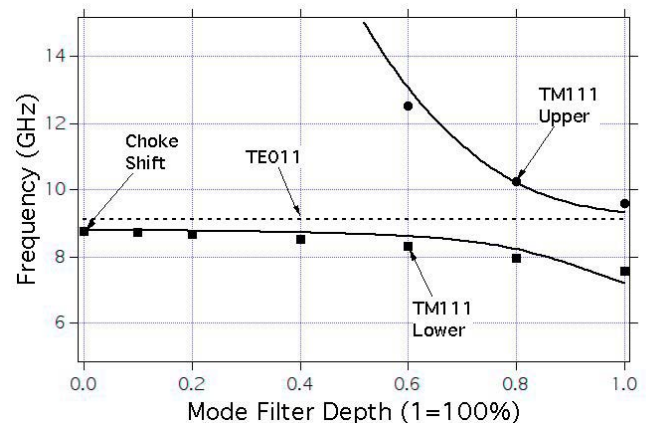


Figure 11. Modeled TM_{111} frequency as a function of mode filter depth. The dashed line shows the TE_{011} mode, which is unaffected by mode filter depth. A depth of “1” corresponds to the design depth. Dots are the values for the upper and lower TM_{111} modes determined in the numerical analysis, while lines are simultaneous fits using a derived functional form. The good agreement supports the identification of the TM_{111} modes in the measurable mode filter depth of 1. Note the break in degeneracy between the TM_{111} mode and the TE_{011} mode even when no mode filter is present (zero depth).

Microwave Cavity Fabrication

The two TE_{011} cavities need to be reasonably matched in center frequency with minimal thermal gradients between them, so it is therefore necessary to use a fabrication process that will suppress irreversible frequency changes due to drift or bakeout. In addition the fabrication method must allow for inspection of internal dimensions. A process combining electro-forming and machining with iterative annealing cycles was chosen.

In this approach to cavity fabrication, a mandril that matches the interior dimensions of the cavity is carefully machined out of aluminum. A copper wall and endcaps are machined as well, however this is done in several steps. First a rough cut is made, then the parts are annealed and then a final fine cut is made. In principle, far less stress will be built into the pieces on this final step than if the parts were machined all at once with no intervening anneal. Since it is likely that residual machining stress is the cause of dimensional creep within copper structures, this too should be reduced. After machining, the parts are then assembled onto the mandril and “cold braised” using the electro-forming process as the joining method. The mandril provides a way of making a precision inspection on what is to become an interior dimension. The machine-anneal-machine method reduces the amount of residual stress in the parts thereby reducing the primary source of frequency drift and the electro-forming joining process eliminates dimensional distortion due to heating to braze temperatures. As seen in Fig. 12 the predicted and measured values of modes near the primary TE_{011} mode are in good agreement giving further confidence in the model and the fabrication process. The two prototype cavities fabricated using the fabrication method described above resonated at 1.04 and 1.21 MHz respectively below the design value. This corresponds to approximately 2.5 μm of

machining error, well within the $\pm 5 \mu\text{m}$ specification. In both cavities a Q of about 22,000 was measured for the TE₀₁₁ mode, which is close to the theoretical value indicating no gross imperfections in the internal cavity surfaces. The TM₁₁₁ modes were found at the right frequencies with the predicted Qs indicating that machining of the difficult to inspect mode filters was done correctly.

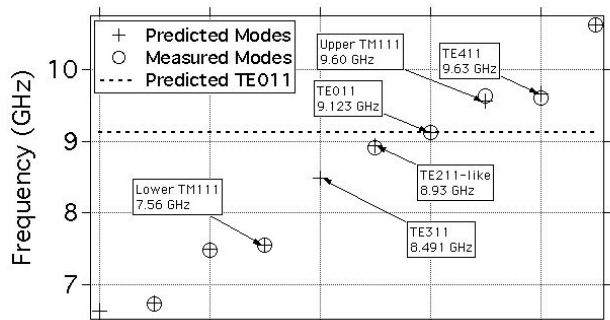


Figure 12. Frequencies for the modes closest to the primary TE₀₁₁ mode.

To simulate a vacuum bakeout both cavities were cycled multiple times to 200 C for 5 days (each cycle). In each case, the cavities shifted by between 100 and 150 kHz after the bake was complete. This is marginally within the requirement, which states that each cavity must remain within 1/2 linewidth (about 230 kHz) of the other after the vacuum bakeout. In addition, there were indications in one cavity of a time lag between temperature changes and frequency response. The cavities were next cycled to 400 C for one day. This temperature was outside the specified range that they are supposed to handle and as expected, the shift was larger after the cycle: -1.6 MHz for one and -0.9 MHz for the other. While this shift left the two cavities off of their specified frequency, the 400 C cycle eliminated the time lag in frequency response to temperature and subsequent cycles to 200 C resulted in no further frequency shift within the measurement resolution of 50 kHz. It is possible that residual stresses still present were responsible for the time lag in the frequency response to small temperature changes after the initial 200 C cycles and that the 400 C cycle simply did a better job of annealing at the price of a large frequency shift. This result suggests that a higher anneal temperature during the intermediate manufacturing step may be advisable. Even without this change however, the cavities were within specification and this fabrication method is viewed as viable.

CONCLUSIONS

Details of the magnetic, vacuum and microwave designs for the PARCS CPP that meet their respective requirements, along with analyses and tests to support those designs, have been presented. As of this writing, due to changes in NASA priorities, PARCS is no longer a flight project and no further work is being performed on its design. However, one goal of the PARCS project was to advance the state of knowledge of advanced frequency standards. As such, much of what was

learned while developing its design is applicable to other laser-cooled clocks, both terrestrial and space-based.

ACKNOWLEDGMENTS

John Dick at JPL, together with the authors, led the design of the microwave interrogation region of the CPP and provided invaluable technical insight. The extensive finite element modeling and development of implementation approaches for the microwave design was performed by Dan Hoppe and Behrouz Khayatian at JPL. Bob Glaser at JPL was instrumental in determining the successful method for the microwave cavity fabrication and was responsible for designing, building and testing the prototype atom shutter. Glaser together with Andy Stone at JPL took high-level requirements and turned them into a workable CPP mechanical configuration. The authors would also like to acknowledge many useful discussions with the entire JPL and NIST development teams for PARCS, especially, Dave Brinza and Dave Seidel at JPL and Elizabeth Donley and Tom Heavner at NIST.

REFERENCES

- [1] D.U. Gubser et al., *Rev. Sci. Instrum.* **50**, 751 (1975).
- [2] A theorem has been proven, which states that between any two field values the optimal adiabatic ratio (where optimal means the largest minimum value over the interval) is obtained by a field that has a 1/z dependence subject to the two boundary conditions. E.A. Burt, manuscript in preparation.
- [3] J.H. Shirley and S.R. Jefferts, *Proc. 2003 IEEE International Frequency Control Symposium*, p. 1072 (2003).
- [4] C.W. Beer and R.A. Bernheim, *Phys. Rev. A* **13**, 1052 (1976).
- [5] N.D. Bhaskar et al., *IEEE Trans. Ultra. Fer., Freq. Cont.* **37**, 355 (1990).
- [6] C. Benvenuti, et al., *Vacuum* **50**, 57 (1998).
- [7] C. Benvenuti, et al., *J. Vac. Sci., Technol. A* **16**, 148 (1998).
- [8] C. Benvenuti, et al., *Vacuum* **53**, 219 (1999).
- [9] C. Benvenuti, et al., *Vacuum* **60**, 57 (2001).
- [10] C. Benvenuti, private communication.
- [11] Varian Star Cell 20 l/s model 9190261 - pumping speed values are taken from the 2000 Varian catalog, p. 106 and p. 120.
- [12] For example, O'Hanlon, *A User's Guide to Vacuum Technology*, p. 36.
- [13] D.H. Davis, *J. Appl. Phys.* **31**, 1169 (1960).
- [14] M. Minato et al., *Vacuum* **47**, 683 (1996); M. Minato, *J. Vac. Sci. Technol. A* **13**, 540 (1995); Y. Koyatsu et al., *Vacuum* **47**, 709 (1996); Watanabe et al., *J. Vac. Sci. Technol. A* **13**, 2587 (1995).
- [15] Outgassing rates for O₂ and N₂ are generally not discussed in the literature because they are usually dominated by H₂, CO, CO₂ and CH₄. In this analysis we use a conservative upper bound of 1×10^{-15} Torr-l/s-cm² (equal to that of CO) for these two gasses.
- [16] A. Roth, *Vacuum Technology*, second revised edition, p. 168.
- [17] W.M. Klipstein, et al., *Proc. 2001 IEEE IFCS* P. 25 (2001).
- [18] G.J. Dick, et al., *Proc. 2003 IEEE IFCS*, p. 1032 (2003).
- [19] N.F. Ramsey, *Molecular Beams*, Oxford University Press (1956), p. 132.
- [20] S.R. Jefferts, et al., *Proc. 1998 IEEE IFCS* p. 6 (1998).
- [21] S.R. Jefferts, J.H. Shirley, N. Ashby, E.A. Burt and G.J. Dick, manuscript submitted to the *IEEE Trans. Ultra. Fer. Freq. Cont.*
- [22] D.G. Enzer and W.M. Klipstein in this proceedings.
- [23] Ph. Laurent, et al., *Proceedings of the 1999 Joint Meeting EFTF-IEEE IFCS*, p. 152 (1999).
- [24] S.R. Jefferts et al., *Metrologia* **39** (2002) pp. 321-336.